

# CFD Study of a Wing in Close Proximity to a Flat and Wavy Ground Plane

E.M. Smuts<sup>a</sup> and A.T. Sayers<sup>a</sup>

Received 23 February 2011 and accepted 1 December 2011

*A three-dimensional computational fluid dynamics (CFD) model of a rectangular DHMTU wing of aspect ratio 3 was created to investigate the performance of the wing operating in close proximity to a moving ground plane. The model was created in the commercial software package, Fluent<sup>®</sup>, using an implicit, pressure-based, segregated solver together with the Spalart-Allmaras turbulence model. Initially, the wing was tested in the presence of a flat moving ground plane. The lift, drag and pitching moments of the wing were measured at a Reynolds number of  $2.21 \times 10^5$  for relative ground clearances of  $0.06 < h_0 < 1.03$ , and angles of attack between 1 and 13 degrees. These results were compared to experimental data to determine the accuracy of the numerical model. The model was found to be sufficiently accurate, and so was adapted to incorporate a sliding mesh in order to simulate the motion of waves in the ground plane. Wavelengths of 1 to 4 times the chord length were tested, with maximum wave heights being limited to  $1/7^{\text{th}}$  of the wavelength. The wavy ground plane model performed well, reliably producing force coefficient variations that were altered by the different wave profiles.*

**Additional Keywords:** Ground effect, turbulence models

## Nomenclature

### Roman

|       |  |
|-------|--|
| $AR$  | aspect ratio ( $b/c$ )                       |
| $A$   | plan area of the wing ( $= bc$ )             |
| $a_w$ | wave amplitude                               |
| $b$   | wing span                                    |
| $c$   | wing chord                                   |
| $C_D$ | drag coefficient ( $= D/0.5\rho v^2 A$ )     |
| $C_L$ | lift coefficient ( $= L/0.5\rho v^2 A$ )     |
| $C_M$ | moment coefficient ( $= M/0.5\rho v^2 A c$ ) |

|       |   |
|-------|---|
| $D$   | drag  |
| $h$   | ground clearance, measured between the ground and the trailing edge of the wing |
| $h_0$ | relative ground clearance ( $= h/c$ )   |
| $L$   | lift  |
| $L_w$ | relative wavelength ( $\lambda/c$ )   |
| $M$   | pitching moment   |
| $Re$  | Reynolds number ( $= \rho V c / \mu$ )  |
| $t$   | maximum thickness of the wing   |
| $V$   | free stream velocity  |
| $x$   | distance along chord from leading edge  |

### Greek

|           |                               |
|-----------|-------------------------------|
| $\alpha$  | angle of attack               |
| $\lambda$ | wavelength                    |
| $\mu$     | free stream dynamic viscosity |
| $\rho$    | free stream density           |
| $\varphi$ | phase angle                   |

## 1. Introduction

Ground effect is a phenomenon that is well known to all aircraft pilots as the tendency of their aircraft to “float” in the air as they approach the ground during landing. Conversely, it is also the effect that some pilots exploit to aid take-off. Ground effect technology was being studied as early as the 1920’s, and in 1935, Finnish engineer Kaario designed and constructed a craft which was able to take advantage of the ground effect<sup>1</sup>. Russian, Rostislav Alekseev, and German, Alexander Lippisch, made significant contributions to the field throughout the Cold War era. The Russian *Ekranoplans* (*ekran* - screen, *plan* - plane) were flying behemoths, over 100m long and weighing up to 550 t. They could travel at speeds over 400 km/h, just a few meters above the ground. Vehicles that take advantage of ground effect have come to be known as wing-in-ground effect, or WIG, vehicles. Large WIG craft can have high lift/drag ratios of 15 to 30.

Based on the fact that WIG craft spend most of their flying time over open water, this study concerned itself with the development of a computational model that would accurately model the flow around a wing in the presence of a wavy ground plane. Validation of numerical models is usually achieved by comparing the results to equivalent experimental data. However, there is very little experimental data available on wings in ground effect, particularly of lifting wings and wings in the presence of waves. Fortunately, data was available for a wing in the presence of a flat ground plane. Therefore it was decided to first develop a flat ground plane model that could reproduce the experimental data. The flat ground plane

<sup>a</sup> CERECAM, Department of Mechanical Engineering, University of Cape Town, Rondebosch, 7700. South Africa.  
E-mail: Anthony Sayers@uct.ac.za

model was then adapted to model wave motion within the ground plane.

The following sections discuss the development of the model for the wavy ground plane. Initially, the model for the flat ground plane is presented and compared against the experimental data of Rhodes<sup>2</sup>. Following from this model, the design of the wavy ground plane model is described. The success of this model is then discussed in relation to the flat ground plane model.

## 2. Flat Ground Plane Model

The experimental data of Rhodes<sup>2</sup> was used to validate the flat ground plane model. He measured lift, drag and pitching moments of the wing at varying angles of attack and ground clearances.

Rhodes made use of a DHMTU 10-40-2-10-2-60-21-5 rectangular airfoil. It had a span,  $b$ , of 465 mm and a chord,  $c$ , of 155 mm, resulting in an aspect ratio of 3. The relatively slender wing had a 10 % maximum thickness ratio ( $t/c$ ) at a chordwise position from the leading edge,  $x/c = 40$  %. The wing had a flat section on the lower surface from  $x/c = 10$  % to  $x/c = 60$  %. The flat section was parallel to the chord and 2 % below it. The nose radius parameter was 5. Figure 1 gives an indication of these variables.

Flow over a simple airfoil like this wing is known to be symmetric. Therefore only half the wing was modelled.

Aerodynamic changes due to ground effect usually only become significant for ground clearances less than the length of the chord. For this reason, the ground clearance is usually non-dimensionalised relative to the chord of the primary lifting surface. The relative ground clearance is denoted as  $h_0 = h/c$  where the ground clearance,  $h$  is measured from the trailing edge of the wing, and  $c$  is the mean aerodynamic chord of the wing.

Four relative ground clearances of 0.06, 0.12, 0.50, and 1.30 were tested in order to determine the model's ability to distinguish between small and large clearances between the wing and ground plane. WIG wings are unlikely to operate at negative angles of attack ( $\alpha$ ), and most CFD codes have difficulty in resolving the turbulence generated at high  $\alpha$ .

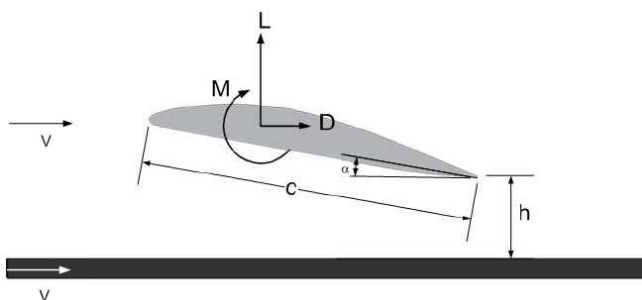


Figure 1: Variables affecting the wing in ground effect

Therefore the angle of attack was limited to between 1° and 13°, in 2° increments.

Rhodes' experiments were conducted at a Reynolds Number of  $2.21 \times 10^5$ , resulting in an inlet air velocity of 20.827 m/s. The ground plane velocity corresponded with the inlet air velocity.

## 3. Numerical Modelling of Ground Effect

This section outlines the numerical model created to simulate the wing in the presence of a flat ground plane.

### 3.1 Mesh generation

The requirement of a flat ground plane favoured a flow domain shaped like a rectangular prism, where a fully structured, orthogonal mesh could be used since the cells could be easily aligned with the boundaries of the domain. Figure 2 shows the front (left) and side views (right) of the domain along with the dimensions of the computational domain relative to the wing (side view not drawn to scale). The domain extends only 6.45 chord lengths upstream, but as far as 19.35 chord lengths downstream to allow the trailing vortices to develop properly. The spanwise dimension (5.2 chord lengths) needs to be longer than the vertical dimension (3.9 chord lengths) due to the trailing vortices.

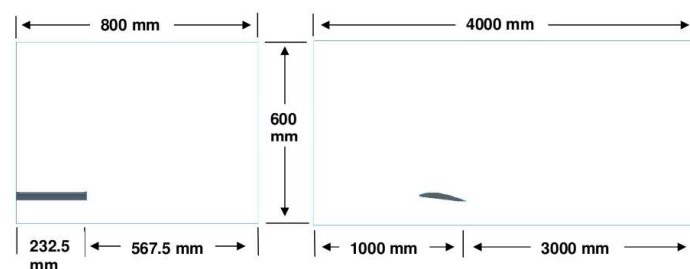


Figure 2: Computational domain

As the resolution of the boundary layer around the wing was important, structured cell layers were wrapped around the wing. This gave excellent control of the boundary layer mesh.

The irregular geometry of the wing, and its boundary layer mesh, did not suite the same orthogonal structured mesh that was used in the rest of the domain. Therefore an irregular, unstructured mesh was used to merge the orthogonally aligned mesh of the domain with the structured mesh around the wing.

Unstructured meshes are not ideal, since they can introduce inaccuracy into the solution through numerical diffusion when the flow becomes misaligned with the cell faces. However, it was felt that the structured boundary layer mesh around the wing would provide sufficient accuracy in the important flow regime that is in contact with the wing. The ground plane mesh that surrounds the wing can be seen in figure 3.

The mesh density around the wing resulted in 150 cells being placed on the wing's upper surface and 72 on its lower surface (leading edge to trailing edge). During grid dependency

tests, it was found that these cells worked best if concentrated around the leading edge to capture the flow as it split around the nose of the wing. Along the span of the wing, 34 cells were used. These cells were concentrated towards the wingtip.

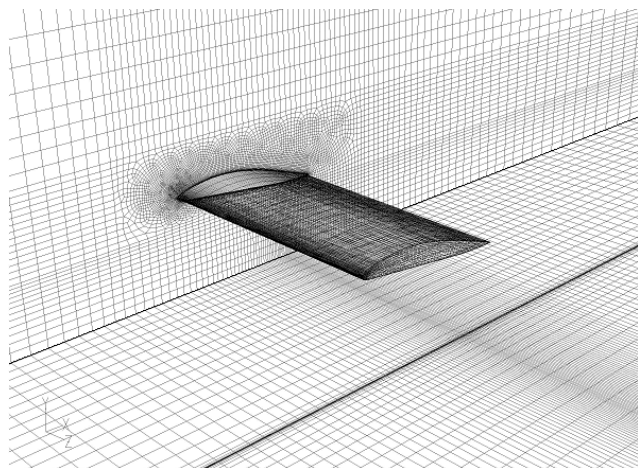


Figure 3: Ground plane mesh

### 3.2 Boundary conditions

The numerical model was required to duplicate the wind tunnel setup used during the experiments. The resulting boundary conditions are discussed below and their numbered positions are illustrated in Figure 4. The inlet face (ABDC) was modelled as a velocity inlet, where velocity, scalar, and turbulence properties were specified. The outlet face (EFHG) at the exit of the domain was modelled as an outflow boundary, which assumed a zero normal gradient for all of the flow variables, except pressure. As the flow problem was symmetric, the plane through the centre of the wing was specified as a symmetric boundary (ACGE). Here, the velocity components normal to the boundary, as well as

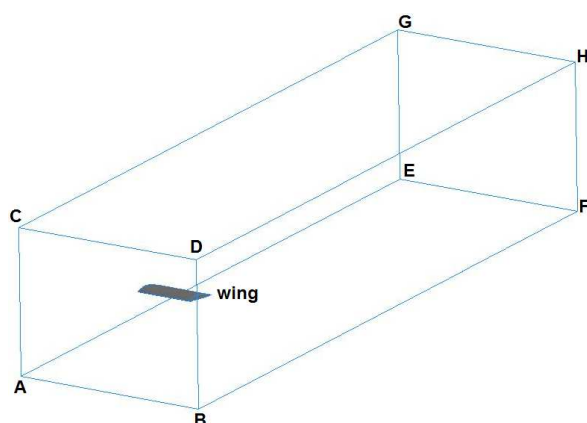


Figure 4: Domain boundary conditions

the gradients of any other variable, were set to zero, i.e. zero flux crosses the boundary. The lower face, which represents the ground plane (ABFE), was modelled as a solid wall boundary with the “no-slip” condition specified. The wall was given a translational velocity to match the velocity of the airflow. The wing itself was also modelled as a wall boundary to create a solid body. The two remaining faces (BDHF and CDHG) were specified as velocity inlets. It was assumed that these boundaries were far enough away from the wing to exhibit free stream conditions.

### 3.3 Turbulence modelling

The Spalart-Allmaras (SA) turbulence model was used. This one-equation model was originally developed for aerospace applications that involved wall-bounded flows<sup>3</sup>, and as a result, is particularly well suited for airfoil applications. It has also been shown to give good results for boundary layers that are subject to adverse pressure gradients<sup>3</sup>. In particular the SA model used in this study was modified to include “strain/vorticity based production” with the intention that the model would be better equipped to predict the turbulence generated by the swirling flows near the wingtip. The original SA model was effectively a low-Reynolds number model which required the viscous affected region of the boundary layer to be properly resolved. This meant that a fine mesh was required to correctly resolve the boundary layer.

Other possible turbulence models considered for this study were the k-ε realizable and k-ω SST models. However, during initial tests for two-dimensional flow over an NACA 2612 airfoil in a free stream, the SA model provided the best and most reliable results when compared to the k-ε and k-ω models. Thus, not only was the SA model less computationally expensive than the two-equation k-ε and k-ω models, but it was also more accurate.

The transport equation for the SA model is given in equation 1. The transported variable  $\tilde{\nu}$  is identical to the turbulent kinematic viscosity, except for in the near wall (viscous affected) region. In this equation,  $G_\nu$  is the production of turbulent viscosity,  $Y_\nu$  is the destruction of turbulent viscosity that occurs in the near wall region due to wall blocking and viscous damping,  $\sigma_\nu$  and  $C_{b2}$  are constants,  $\nu$  is the molecular kinematic viscosity and  $S_\nu$  is a user-defined source term. The model constants are provided in Table 1.

$$\frac{\partial}{\partial t}(\rho\tilde{\nu}) + \frac{\partial}{\partial x_i}(\rho\tilde{\nu}u_i) = G_\nu + \dots$$

$$\dots \frac{1}{\sigma_\nu} \left[ \frac{\partial}{\partial x_j} \left\{ (\mu + \rho\tilde{\nu}) \frac{\partial \tilde{\nu}}{\partial x_j} \right\} + C_{b2} \rho \left( \frac{\partial \tilde{\nu}}{\partial x_j} \right)^2 \right] - Y_\nu + S_\nu \quad (1)$$

|             |        |
|-------------|--------|
| $C_{b1}$    | 0.1355 |
| $C_{b2}$    | 0.662  |
| $C_{v1}$    | 7.1    |
| $C_{w2}$    | 0.3    |
| $C_{w3}$    | 2      |
| $C_{prod}$  | 2      |
| Prandtl No. | 0.667  |

Table 1: Spalart-Allmaras turbulence model constants

Using the SA model required  $y^+$  values between 1 and 5 for the first cell in contact with the solid boundary. A first cell height of 0.2 mm was used, which resulted in  $y^+$  values of 1 to 4 occurring over the surface of the wing. This included the wingtip. The boundary layer in contact with the ground plane was less important than that of the wing. Only at  $h_0$  values of 0.06 and 0.12 was an attempt made to model the boundary layer of the ground plane.

### 3.4 Solver settings

Since the WIG model problem was that of a low-speed incompressible fluid, a pressure-based, implicit solver was suitable. A segregated solver was used to solve the governing equations sequentially. The lower memory requirement of a segregated solver, versus a coupled solver, meant that double precision accuracy could be used in the solution.

The SIMPLE algorithm was used to couple the pressure and velocity fields. The standard pressure discretisation scheme was used, in conjunction with a second order upwind scheme for the momentum equations, and a first order upwind scheme for the modified turbulent viscosity.

### 3.5 Residuals and convergence

Residuals of mass, velocity, and turbulent viscosity were monitored for convergence. When these residuals dropped below a value of  $1 \times 10^{-4}$ , the solution was deemed to have converged.

## 4. Wavy Ground Plane Model

Due to the relative success of the flat ground plane model (see section 5), this model was adapted to include the movement of waves in the ground plane.

### 4.1 Waves in the ground plane

The wavelengths were chosen to be multiples of the wing chord length, resulting in an  $L_w$  of 1, 2, 3, and 4. The heights of the respective waves were chosen as fractions of the wavelength. Since the maximum height of a wave is limited to 1/7th of the wavelength<sup>4</sup>, this set the upper limit for the wave heights. For the longer wavelengths, smaller wave heights were also used in order to compare waves of different wavelengths while keeping the wave height the same. Table 2 gives the wave height ratios relative to the

ground clearance,  $h$ , and the wavelength. The wave amplitude,  $a_w$ , is half of the total wave height.

| Total Wave Height (mm) | Relative Wave Height ( $a_w/h$ ) | Total Wave Height relative to Wavelength |      |      |      |
|------------------------|----------------------------------|--|------|------|------|
|                        |                                  | 1  | 2    | 3    | 4    |
| <b>22.143</b>          | 0.143                            | 1/7                                      | 1/14 | 1/21 | 1/28 |
| <b>44.286</b>          | 0.286                            |  | 1/7  | 2/21 | 1/14 |
| <b>66.429</b>          | 0.429                            |  |      | 1/7  | 3/28 |
| <b>88.572</b>          | 0.571                            |  |      |      | 1/7  |

Table 2: Suitable wave heights to wavelength ratios

There were two very different methods of introducing waves into the domain. A multi-phase model could have been used to introduce actual waves of water flowing through the lower portion of the domain. Another method would be to create a solid boundary with a wavy profile that could move past the wing like a set of waves. This latter method could be accomplished through the use of a sliding mesh. According to Rozhdestvensky<sup>5</sup>, the deformation of the water's surface due to the presence of the WIG craft can be considered negligible, because the density ratio between air and water is so low that the water's surface behaves as if it were solid. Therefore the waves could be modelled as a solid surface in the sliding mesh model.

A multi-phase model required a fine grid to resolve the water's surface, as well as extra variables in the governing equations would have to be solved. A sliding mesh model would also require extra cells in the domain. Unlike the multi-phase model however, the waves would be modelled as a solid boundary and air would be the only fluid in the entire domain, thus resulting in a much simpler problem. A simpler problem is usually less computationally expensive, and so the sliding mesh method was used.

### 4.2 Sliding mesh model

The new model incorporated an extra mesh region directly below the original domain which contained the waves. This new region would form the sliding mesh region. The mesh for the  $h_0 = 0.06$  ground clearance would be used for the stationary region as this allowed the entire waveform of the highest waves to fit into the new sliding region while maintaining the correct clearances between the wing trailing edge and wave centre line. The addition of this new region is illustrated in Figure 5.

To replicate the motion of the waves past the wing, the sliding region would translate along the bottom of the original domain. It was assumed that the wave velocity would be small relative to the wing velocity. Therefore the sliding region was made to translate at the same speed as the free stream velocity, namely 20.827 m/s.

The sliding region could only be of finite length. A longer region would allow more of an overlap between the two mesh

regions, but would increase the number of cells in the model. Thus a two-dimensional version of the model

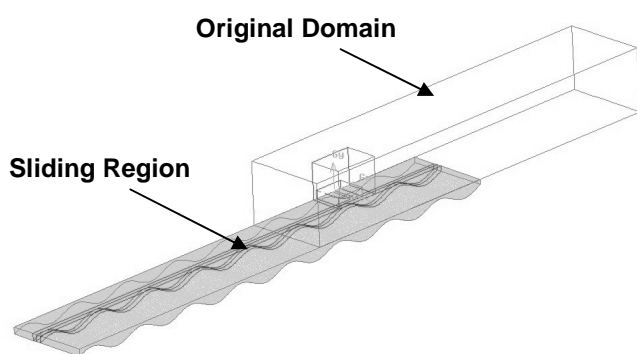


Figure 5: Original domain with new sliding region

was tested to determine the minimum domain length as well as the start and end positions of the sliding region that would not significantly affect the flow around the wing. Disturbances upstream of the wing would be of primary concern. Final dimensions of the region are given in figure 6. The sliding region was 5 m long, stretching out 4 m in front of the trailing edge of the wing while in the start position. The region would translate 2.5 m, which would require a solution time of 120 s. This provided sufficient time for the force coefficients to settle and converge to similar values for successive wave oscillations.

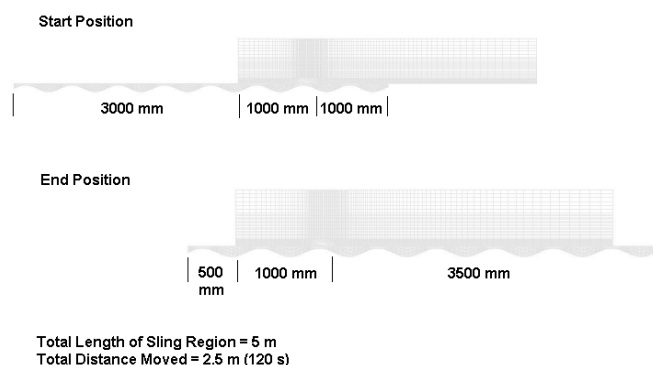


Figure 6: Streamwise dimensions of sliding region showing start and end positions

Furthermore, the mesh density in the vertical and streamwise directions was also tested. It was found that a cell distribution of 400 cells (streamwise) by 14 (vertical) cells would be adequate, as this mesh produced similar results to a 500 x 16 mesh. The resulting mesh is illustrated in figure 7. The spanwise distribution of cells was kept the same as for the stationary domain. This was done in an attempt to reduce the error incurred when the values were interpolated across the interface between the two regions.

However, the spanwise distribution of cells was changed from that of the original flat ground plane model to limit problems of high turbulent viscosity. The new cell distribution was found to be equivalent to the original mesh.

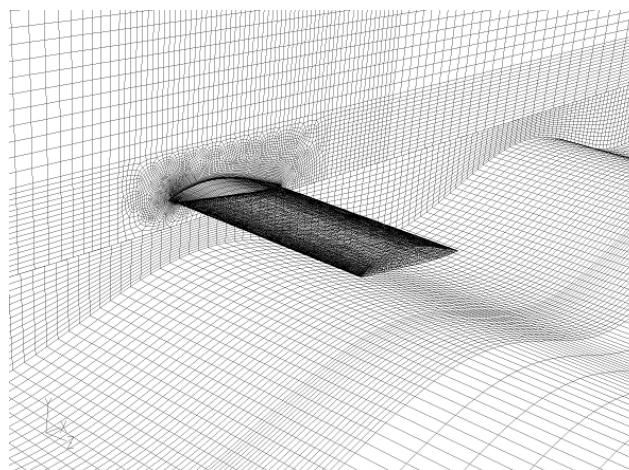


Figure 7: Resulting mesh around wing due to sliding region

## 5. Results for the Flat Ground Plane

The results from the flat ground plane CFD model are compared to those of Rhodes<sup>2</sup> and analysed in such a way so as to determine the effectiveness of CFD to properly re-create the experimental results, and its suitability for use in further work on ground effect airfoils. Experimental data for  $\alpha$  of  $-1^\circ$  and  $15^\circ$  have been included in all graphs comparing experimental results to CFD in order to further indicate the trends of the experimental data.

### 5.1 Lift coefficient, $C_L$

Figure 8 shows experimental and CFD  $C_L$  values plotted against  $\alpha$  for the flat ground plane. Most of the  $C_L$  values were within 10 % of Rhodes' experimental values. However, for angles of attack of  $1^\circ$  and  $3^\circ$ , many of the values showed a difference of more than 20 %. For  $h_0$  values of 0.06 and 0.12, the values at the low angles of attack of  $3^\circ$  and  $5^\circ$  were generally more accurate. However, as the wing angle increased, the error became greater. Interestingly, the converse is true for the two higher ground clearances, as the errors reduced to within 5 % for some cases. A trend that seems to apply for all ground clearances is that the errors range from underestimating the lift at low angles, to overestimating them at the higher angles.

### 5.2 Drag coefficient, $C_D$

CFD was incapable of determining the drag on the airfoil to any reasonable degree of accuracy. In many cases ( $1^\circ$  to  $7^\circ$ ) the

error was more than 50 %, while the error only marginally improved as the angle of attack was increased.

up the correct behaviour of the pitching moments. If the drag values were correct, then the  $C_M$  values would match closely.

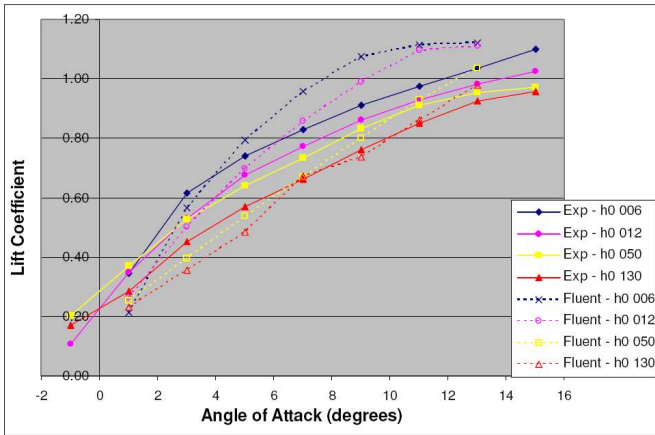


Figure 8: Experimental and CFD lift coefficient versus angle of attack at constant  $h_0$

### 5.3 Pitching Moment Coefficient, $C_M$

The pitching moment coefficient was calculated about the  $\frac{1}{4}$  mean aerodynamic chord position. Figure 9 shows these values plotted against  $\alpha$ . Wing pitching moments are a result of the lift and drag forces generated by the wing (and their respective positions). Initially, where both the lift and drag values at low  $\alpha$  are smaller than the experimental values, the magnitude of the  $C_M$  is much lower than the experimental values. As the lift and drag values rise above the experimental values, the  $C_M$  values move closer to the experimental values. Therefore the CFD model is picking

### 5.4 Increased static pressure under the wing

One of the reasons that WIG wings generate more lift than conventional wings is that as the wing moves closer to the ground the air becomes trapped under the wing<sup>1</sup>. The resulting increase in pressure aids the wing in generating more lift. This characteristic is illustrated in Figure 10, where the static pressure distribution around the wing and symmetry plane is given for each of the four ground clearances. Each frame is taken from below and in front of the wing, looking towards the symmetry plane. The wing is at  $7^\circ$ . The contours denote gauge pressure in Pascals.

The pressure rise is most notable in the vicinity of the leading edge, and toward the centreline of the wing. It is this higher pressure under the wing that gives these wings their superior performance at low ground clearances, particularly at clearances below  $0.1c$ . It is also this higher pressure that increases the nose down pitching moment of WIG wings<sup>6</sup>.

### 5.5 Restricted vortex development

In figure 11, the flow pathlines illustrate the size and position of the resulting wingtip vortex for a wing at  $11^\circ$  angle of attack

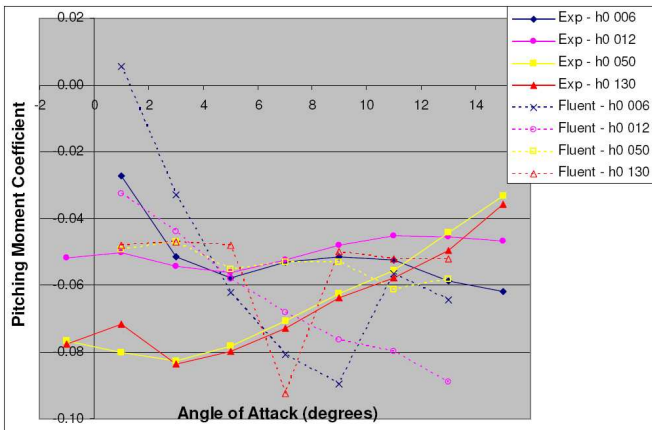


Figure 9: Pitching moment coefficient versus angle of attack at constant  $h_0$

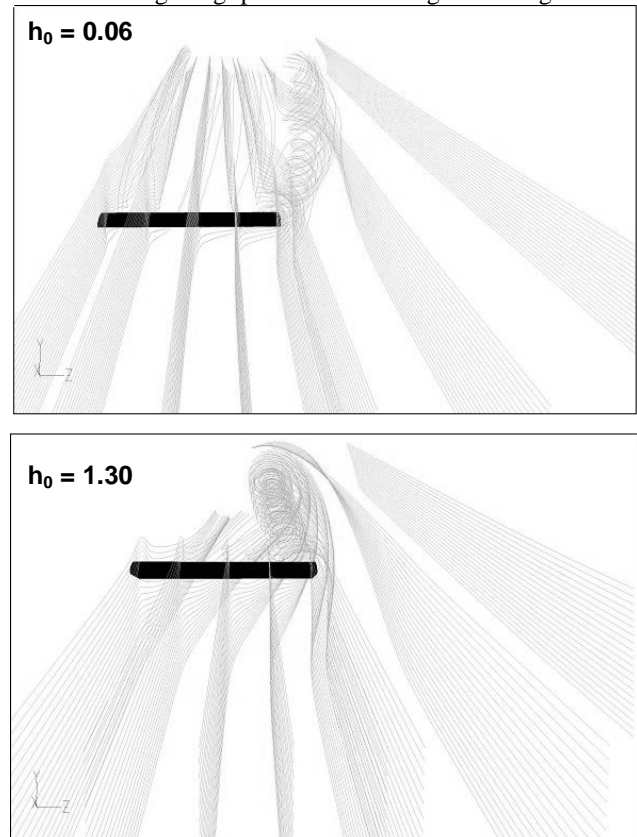


Figure 11: Elevated front view showing vortex position and size change due to changing  $h_0$

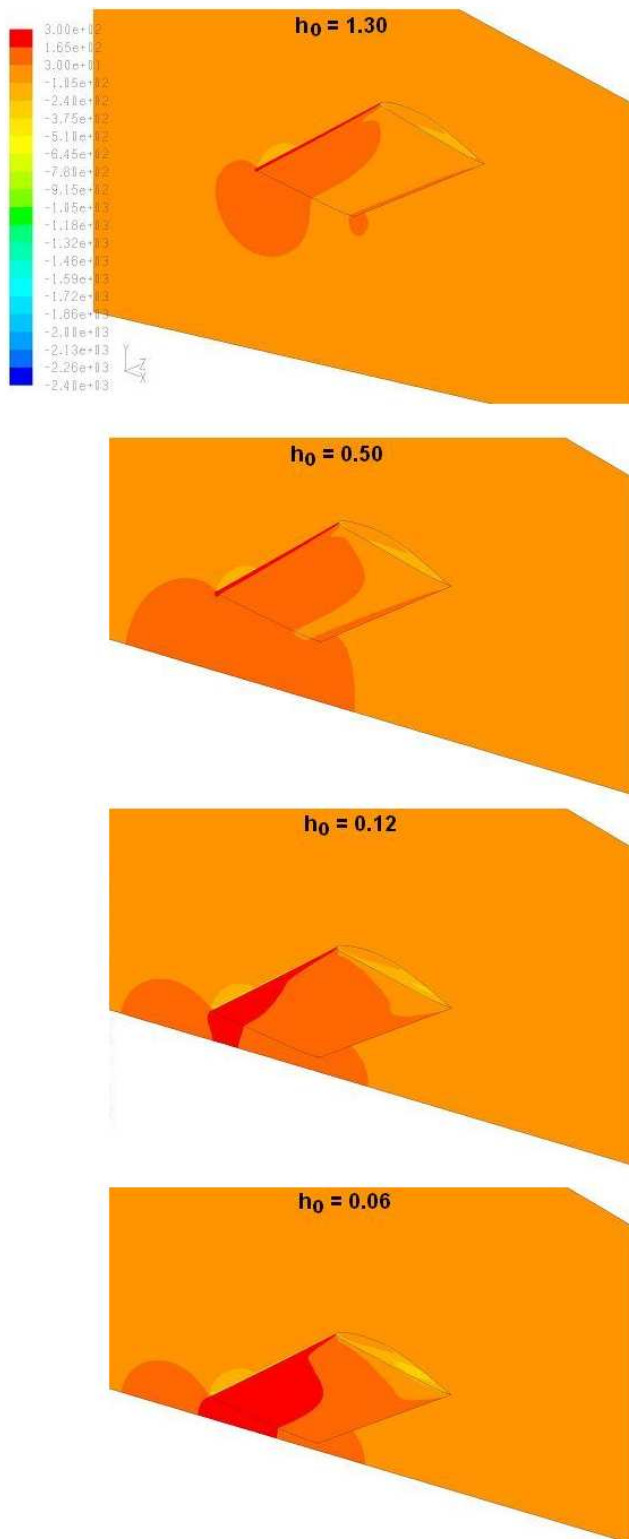


Figure 10: Static pressure contours on the lower surface of the wing for each  $h_0$

at both  $h_0$  of 0.06 and 1.30. Flying in close proximity to the ground limits the development of the wingtip vortices and so reduces their impact on the wing efficiency. For an  $h_0$  of 1.30, the vortex travels straight downwind from the wingtip. However, when the wing is close to the ground, the vortex tends to be pushed outwards and away from the wingtip. High aspect ratio wings are less affected by wingtip vortices, since the vortices are far apart from each other and their interaction is limited<sup>7</sup>. Ground effect produces the same result for low aspect ratio airfoils, as the vortices at the wing-tip are pushed away from each other and so cannot interact as strongly.

The cross-sectional width of the vortex is also affected by the presence of the ground plane. It is not uncommon for the wingtip vortices to grow very large, the further they travel downstream. However, the ground plane restricts the size of the vortex. For the case of  $h_0 = 0.06$ , the vortex does not have sufficient room to develop and thus does not become as wide, or as high, as it would at higher ground clearances.

## 6. Results for the Wavy Ground Plane

To the authors' knowledge, there is no experimental data with which to compare the wavy ground plane CFD results, so any comments on the validity of these results are made in relation to the CFD simulations studied by the author for the flat ground plane.

Simulations were only conducted for angles of attack of  $7^\circ$  and  $11^\circ$ . This gave an indication of the performance trend of the wing over a range of angles of attack. Simulations for an angle of attack of  $1^\circ$  or  $3^\circ$  were not attempted as their respective results for the flat ground plane were not accurate enough to provide reliable results. The simulations were conducted for varying wavelengths and wave heights while a constant clearance of  $h_0 = 0.50$  between the wing and the wave centre line (mean height) was maintained.

Due to the periodic oscillating nature of the wing forces, each of the coefficients are considered in terms of the maximum, minimum, and mean values. In addition, there will be a phase shift between the oscillations of the force coefficient values and the physical wave. This shift is characterised by the phase angle,  $\phi$  (section 6.4)

### 6.1 Lift coefficient, $C_L$

All of the maximum  $C_L$  values obtained for the wavy ground plane are higher than the  $C_L$  values for the flat ground plane. For  $L_W = 1$ , the  $C_L$  increased by only 1 %, but at  $L_W = 4$ , and at the highest wave height, the  $C_L$  value was 7.5 % higher ( $\alpha = 7^\circ$  and  $h_0 = 0.50$ ). While the minimum  $C_L$  is lower than the  $C_L$  for the flat ground plane, the average  $C_L$  value is higher. The average  $C_L$  value increases as the wavelength and wave height are increased. This is because the maximum  $C_L$  values grow in magnitude much quicker than the minimum values (7.5 % versus 2 % for the  $L_W = 4$  and largest wave height). Therefore this wing, on average, generates more lift in the presence of a wave than for the flat ground plane. This trend was identified

by Rozhdestvensky<sup>1</sup>. For  $\alpha = 11^\circ$ , the peak  $C_L$  value at  $L_W = 4$  is only 6.5 % higher.

When plotting  $C_L$  against  $L_W$  (for constant wave heights),  $C_L$  increases slightly with increasing wavelength (Figure 11). The increase in  $C_L$  is greater for higher wave heights, where the larger changes in wave geometry lead to larger changes in the wing's response. Furthermore, as the wavelength reduces, so the  $C_L$  value tends towards the flat ground plane value (for that  $\alpha$  and  $h_0$ ).

As the wave height reduces, the  $C_L$  tends towards the value for the flat ground plane. This should be expected since as the wave height reduces to zero, so the wave resembles a flat ground plane. Furthermore, the wing is found to be more sensitive to changes in wave height (for constant wavelength) than changes in wavelength (for a constant wave height).

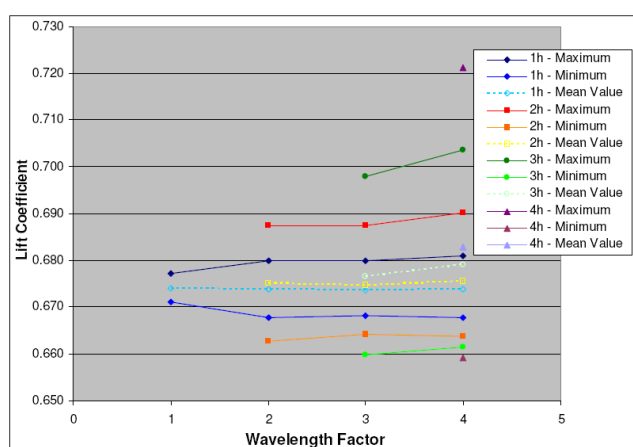


Figure 11: Lift coefficient versus relative wavelength ( $L_W$ )

### 6.2 Drag coefficient, $C_D$

The  $C_D$  values were the same as those obtained for the flat ground plane. There was no apparent trend to the values, and since the magnitude of the values hardly changed from one set to another, no clear trend was shown.

### 6.3 Pitching moment coefficient, $C_M$

The performance of the moment coefficient is again dominated by the performance of the lift coefficient. In general, the  $C_M$  values increased in magnitude for an increasing wave height. An increase in the wavelength (for the same wave height) also increases the pitching moment. As the wing encounters the peaks in the ground plane, the  $C_M$  becomes more negative, increasing the nose down pitching moment of the wing. Alternatively, as the wing flies over the troughs, the  $C_M$  becomes less negative. When these oscillations are averaged out, they show that an

increase in wave size (both wave height and length) slightly increases the nose down pitching moment of the wing.

### 6.4 Phase angle

The phase angle was derived from the phase shift between the force coefficient curve and the wave profile. The phase shift, illustrated in Figure 12, was slightly different for all force and moment coefficients. However, due to the unreliability of the drag values, only the phase angle of the  $C_L$  will be discussed. The phase angles for both the minimum and maximum  $C_L$  values are nearly identical. For the two longer wavelengths, the phase angles are negative, which indicates a leading phase. This means that the peak  $C_L$  values occur before the peak of the ground plane wave. The phase angle then switches to a positive, or lagging, phase angle for  $L_W = 2$ . At a  $L_W = 1$  the phase returns to a leading phase. Similar trends and similar phase angles are found for the wing at  $11^\circ$ .

When plotted against wave height, the phase angle for each wavelength does not change significantly when the wave height is changed. Therefore the phase angle is independent of wave height, and is only affected by the wavelength.

The resulting phase angles are large when viewed in relation to the position of the physical wave under the wing. In some cases, the peak  $C_L$  value is already decreasing while the wave is just beginning to increase in size. Figure 12 shows a typical  $C_L$  curve plotted against the physical wave of  $L_W = 4$ , where the resulting phase shift can be seen.

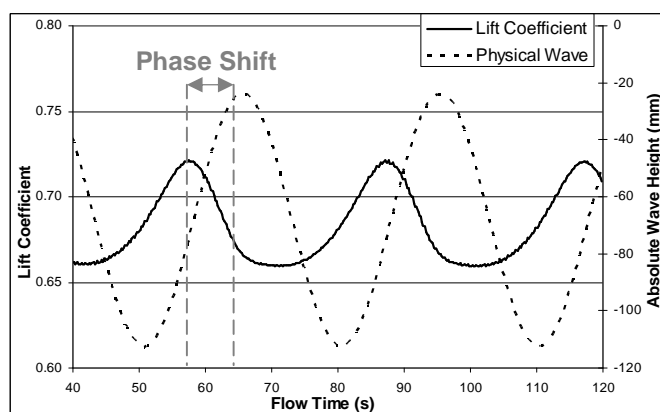


Figure 12: Phase shift of lift coefficient

## 7. Conclusions

The flat ground plane model was successful in recreating the important flow features of a wing in ground effect. The resulting  $C_L$  values were acceptable, with many values falling within 10 % of experimental targets. The poor performance of the  $C_D$  values was of concern, however. The mixed performance of the  $C_M$  was a result of the poor  $C_D$  performance.

A sliding mesh proved to be a simple and reliable method to model waves in the ground plane. The model provided good results in relation to the flat ground plane model. Such large phase angles are not realistic however, though without actual data with which to compare them, their validity could not be determined.

## References

1. *Rozhdestvensky KV*, Wing-in-ground effect vehicles, *Progress in Aerospace Sciences*, 42, 2006, pp. 211-283.
2. *Rhodes SC*, An Experimental Study of the Aerodynamic Characteristics of a Wing in Close proximity to a Moving Ground Plane, MSc Thesis, University of Cape Town, Cape Town, 2006.
3. *Wilcox DC*, Turbulence Modelling for CFD, 2nd ed., DCW Industries, La Canada, California, 1994.
4. *Kinsman B*, Wind Waves – Their Generation And Propagation On The Ocean Surface, Prentice-Hall Inc., New Jersey, 1965.
5. *Rozhdestvensky KV*, Aerodynamics of a Lifting System in Extreme Ground Effect, Springer, Moscow, 2000.
6. *Halloran M and O'Meara S*, Wing in Ground Effect Craft Review, Aeronautical and Maritime Research Laboratory, Melbourne, 1999.
7. *Houghton EL and Carpenter PW*, Aerodynamics for Engineering Students, 4th Ed., Edward Arnold, London, 1993.